



**NATIONAL
OPTICAL
ASTRONOMY
OBSERVATORIES**

Preprint Series

NOAO Preprint No. 861

THE IONIZATION SOURCE IN THE NUCLEUS OF M84

G. A. Bower

R. F. Green

(Kitt Peak National Observatory, National Optical Astronomy Observatories)

A. C. Quillen

(Steward Observatory, University of Arizona)

A. Danks

E. M. Malumuth

(Raytheon ITSS, NASA / Goddard Space Flight Center)

T. Gull

B. Woodgate

(NASA / Goddard Space Flight Center)

J. Hutchings

(Dominion Astrophysical Observatory, National Research Council of Canada)

C. Joseph

(Dept. of Physics & Astronomy, Rutgers University)

M. E. Kaiser

(NASA, Dept. of Physics & Astronomy, Johns Hopkins University)

D. Weistrop

C. Nelson

(Department of Physics, University of Nevada)

To Appear In: The Astrophysical Journal

January 2000

To appear in The Astrophysical Journal

The Ionization Source in the Nucleus of M84¹

G. A. Bower², R. F. Green², A. C. Quillen³, A. Danks⁴, T. Gull⁵, J. Hutchings⁶, C. Joseph⁷,
M. E. Kaiser^{5,8}, D. Weistrop⁹, B. Woodgate⁵, E. M. Malumuth⁴, and C. Nelson⁹

¹Based on observations with the NASA/ESA *Hubble Space Telescope*, obtained at the Space Telescope Science Institute, which is operated by the Association of Universities for Research in Astronomy, Inc. (AURA), under NASA contract NAS5-26555.

²Kitt Peak National Observatory, National Optical Astronomy Observatories, P. O. Box 26732, Tucson, AZ 85726; gbower@noao.edu, operated by AURA under cooperative agreement with the National Science Foundation.

³Steward Observatory, University of Arizona, Tucson, AZ 85721

⁴Raytheon ITSS, NASA/Goddard Space Flight Center, Code 681, Greenbelt, MD 20771

⁵NASA/Goddard Space Flight Center, Code 681, Greenbelt, MD 20771

⁶Dominion Astrophysical Observatory, National Research Council of Canada, 5071 W. Saanich Road, Victoria, BC V8X 4M6, Canada

⁷Dept. of Physics & Astronomy, Rutgers University, P. O. Box 849, Piscataway, NJ 08855

⁸Department of Physics & Astronomy, Johns Hopkins University, Homewood Campus, Baltimore, MD 21218

⁹Department of Physics, University of Nevada, 4505 Maryland Parkway, Las Vegas, NV 89154

ABSTRACT

We have obtained new *Hubble Space Telescope* (HST) observations of M84, a nearby massive elliptical galaxy whose nucleus contains a $\approx 1.5 \times 10^9 M_\odot$ dark compact object, which presumably is a supermassive black hole. Our Space Telescope Imaging Spectrograph (STIS) spectrum provides the first clear detection of emission lines in the blue (e.g., [O II] $\lambda 3727$, $H\beta$, and [O III] $\lambda\lambda 4959, 5007$), which arise from a compact region $\approx 0''.28$ across centered on the nucleus. Our Near Infrared Camera and Multi-Object Spectrometer (NICMOS) images exhibit the best view through the prominent dust lanes evident at optical wavelengths and provide a more accurate correction for the internal extinction. The relative fluxes of the emission lines we have detected in the blue together with those detected in the wavelength range 6295 – 6867 Å by Bower et al. (1998, ApJ, 492, L111) indicate that the gas at the nucleus is photoionized by a nonstellar process, instead of hot stars. Stellar absorption features from cool stars at the nucleus are very weak. We update the spectral energy distribution of the nuclear point source and find that although it is roughly flat in most bands, the optical to UV continuum is very red, similar to the spectral energy distribution of BL Lac. Thus, the nuclear point source seen in high-resolution optical images (Bower et al. 1997, ApJ, 483, L33) is not a star cluster but is instead a nonstellar source. Assuming isotropic emission from this source, we estimate that the ratio of bolometric luminosity to Eddington luminosity is $\sim 5 \times 10^{-7}$. However, this could be underestimated if this source is a misaligned BL Lac object, which is a possibility suggested by the spectral energy distribution and the evidence of optical variability we describe.

Subject headings: BL Lacertae objects: general — galaxies: active — galaxies: elliptical and lenticular, cD — galaxies: individual (M84) — galaxies: nuclei

1. Introduction

Observations of the nuclei of several nearby galaxies have revealed very compelling evidence for massive dark objects with $\sim 10^6 - 10^9 M_\odot$ (see review in Richstone et al. 1998), which are presumably supermassive black holes (BHs). Since black holes of this mass range are strongly suspected to be the central engines powering quasars and AGN, this presents an important opportunity to address several related problems. Determining the local space density of BHs and the host galaxy properties as a function of BH mass should yield important insights into the evolution of quasars as a function of cosmic time and the processes that occur during galaxy formation that might influence BH (and thus quasar) formation. Also, a few of the local BHs reside in galaxies that host an AGN, presenting the opportunity to relate BH mass to other AGN properties (such as radio jets, nuclear emission line regions, and the spectral energy distribution of the central source).

M84 (NGC 4374 = 3C 272.1) is one such nearby BH candidate galaxy with a relatively weak AGN, as indicated by its FR I radio source (Laing & Bridle 1987), an 82 pc diameter nuclear disk of ionized gas aligned approximately perpendicular to the radio jet axis (Bower et al. 1997, hereafter Paper I) whose kinematics indicate the presence of a central $1.5 \times 10^9 M_\odot$ dark compact object (Bower et al. 1998, hereafter Paper II), and a nuclear point source seen in optical images (Paper I). Stellar light profiles in the central few hundred pc of high luminosity elliptical galaxies like M84 are shallow power-law cusps (Faber et al. 1997), suggesting that the sharp nuclear point source in M84 is a distinct entity from the old stellar population. It could represent optical emission related to the AGN powering the radio source, or it could be a nuclear star cluster. Spectroscopy in the far-UV bandpass is sensitive to the presence of hot stars. For example, Maoz et al. (1998) detected far-UV absorption lines from massive stars in a few LINERs with compact UV nuclear sources. However, detecting far-UV emission from M84's nucleus would be difficult since the internal extinction is very high. The purpose of this paper is to determine the nature of the nuclear point source by constraining the ionization mechanism using high spatial resolution STIS spectra of emission lines in the wavelength ranges of 2900 – 5700 Å and 6295 – 6867 Å. Our blue spectrum thus will provide an indirect diagnostic of the possible presence of hot stars by determining if the gas is photoionized by hot stars or a nonstellar continuum.

Since the nuclear point source is embedded in dust, we also utilize near-infrared images of M84 obtained with NICMOS by Quillen, Bower, & Stritzinger (1999), in an effort to measure and to correct for internal extinction. Throughout this paper, we adopt a distance to M84 of 17 Mpc (Mould et al. 1995). At this distance, $1''$ corresponds to 82 pc. The Galactic extinction along the line of sight is $A_B = 0^m13$ (Burstein & Heiles 1984).

2. Observations and Data Calibration

2.1. Spectroscopy

Long-slit spectroscopy of M84's nuclear region was obtained with the STIS CCD, which has a pixel scale of $0''.05/\text{pixel}$ and spatial resolution $\approx 0''.1$ (Kimble et al. 1998; Woodgate et al. 1998), on 1998 April 10. M84's nuclear point source was acquired in the $52'' \times 0''.2$ slit oriented at a position angle (P.A.) of 130° on the sky, while the dust lanes are oriented at P.A. $\approx 60^\circ$ on a scale of $1''$ (Paper I). After target acquisition, we obtained an image through the slit, to verify the slit position. We then obtained spectral observations with the G430L grating, which has a dispersion of $2.73 \text{ \AA}/\text{pixel}$. This grating was set to cover the wavelength range of 2900 \AA to 5700 \AA , which includes several prominent stellar absorption lines (e.g., Mg I b 5167 \AA , 5172 \AA , 5183 \AA , and Ca II H 3968 \AA and K 3933 \AA). The spectral resolution of our instrumental configuration was 10.9 \AA (FWHM), assuming uniform illumination of the slit. The presence of a nuclear point source in optical continuum images implies that our spectral resolution at the nucleus was better than this. Model line spread functions based on pre-flight data predict that the spectral resolution for this observing mode when observing a point source should be between 3.5 \AA at 3500 \AA and 4.0 \AA at 5500 \AA (Walborn & Baum 1998). We integrated for two HST orbits, which was equivalent to 4120 sec. Before the exposure in the second HST orbit, the nucleus was shifted by 4.5 pixels ($0''.225$) along the slit to allow for better rejection of hot pixels during data reduction. A spectrum of the internal wavelength calibration source was obtained intermediate among the galaxy spectra. HST's tracking was very stable during the observation. According to the jitter files reported by the Fine Guidance Sensor, the rms jitter during the observation was 4.8 mas.

The initial steps of the data calibration (bias subtraction, dark rate subtraction, applying the flatfield, and combining the two sub-exposures to reject cosmic-ray events) were completed using the CALSTIS package in STSDAS. The accuracy of the flatfield calibration was 1%. To reject most hot pixels from the data, we constructed a hot pixel mask from dark frames obtained 15 hours before the M84 observations, and then interpolated across these flagged pixels. This interpolation was performed along the dispersion axis, since the flux gradient along the spatial axis near the nucleus is steep (because of the point source). The data were wavelength calibrated and rectified by tracing the Ne and Cr emission lines (in the wavecal) for the dispersion axis and the nuclear point source for the spatial axis, and then applying these solutions for the geometric distortions to the data. The polynomial order of the fit along the dispersion axis was kept low because the S/N in the nuclear point source at $\lambda \lesssim 3500 \text{ \AA}$ is very low (Fig. 1). At this point, spectra from the first and second HST orbits were registered (by aligning on the continuum peak) and then were combined, rejecting any remaining hot pixels. The count rate in each pixel was calibrated to flux in absolute units by applying the standard sensitivity curve for this grating obtained from the HST archive of calibration files. Fig. 1 shows the central region of the reduced two-dimensional spectrum which we analyze in §3.

2.2. Near-infrared Imaging

On 21 July 1998, Quillen et al. (1999) obtained near-infrared images of M84 with the NICMOS Camera 2 (Thompson et al. 1998), which has a pixel scale of $0''.075/\text{pixel}$ (MacKenty et al. 1997). Observations were obtained in each of three broadband filters F110W ($1.10\ \mu\text{m}$), F160W ($1.60\ \mu\text{m}$), and F205W ($2.05\ \mu\text{m}$), corresponding roughly to the J, H, and K bands respectively. The total integration time in each filter was 768 sec. Quillen et al. describe the observing procedure and data reduction only for the F160W image, so we list the details they did not cover for the other bandpasses. For the F205W image, the accuracy of the flatfield is degraded toward the edge of the field of view, and we subtracted the predicted background count rate (MacKenty et al. 1997), which is only a few percent of the count rate from the central few arcseconds of M84. We adopted the flux calibration and photometric zeropoint (i.e., the flux of Vega) provided by the HST pipeline software. The internal photometric error is estimated to be $\leq 2\%$. We did not attempt to transform the NICMOS instrumental magnitudes to standard JHK magnitudes, because the color terms for these observations of M84 in F110W and F205W are significant but are not calibrated very accurately. Since the purpose of these near-IR images is to assess the internal extinction via a color-color plot, it is sufficient to use the NICMOS instrumental system since the effective wavelengths of our filters are known. Fig. 2 shows the near-IR images, which have a resolution (FWHM) of $0''.15$, and two near-IR color maps [i.e., $(J-H)_N$ and $(H-K)_N$], which were formed from the ratios of F110W/F160W images and F160W/F205W images, respectively. The subscript on these colors represents the fact that the magnitudes are in the NICMOS system instead of the Johnson system. The $(H-K)_N$ map shows false color variations toward the edge of the field of view ($\approx 4''$ from the nucleus) symptomatic of the lower quality of the flatfield in F205W. The $(H-K)_N$ color values at pixels within $0''.25$ of the nucleus have not been corrected for the effects of wavelength-dependent resolution. The resolution provided by NICMOS Camera 2 is limited by diffraction at wavelengths greater than $1.75\ \mu\text{m}$ (MacKenty et al. 1997), so the nuclear point source is more extended in the F205W image than in the other bandpasses.

3. Results

As mentioned in §1, the nuclear point source is embedded in dust. We estimate this internal extinction in §3.1. In §3.2, we correct for this extinction and analyze the nuclear spectrum.

3.1. Estimating the Internal Extinction

M84’s nuclear region has been imaged in V and I (Paper I) as well as J, H, and K bands (this paper). We utilize the $(V-H)$ map constructed by Quillen et al. (1999), which provides the longest wavelength baseline where the colors can be converted to the Johnson system. [As discussed in §2, the color term for converting fluxes in the F205W filter to K band magnitudes is significant but

poorly known. The color term for the F160W filter (H-band) is insignificant relative to the internal error (which is the reason we drop the N subscript from the (V–H) color.) However, estimating the extinction from one color requires assuming the standard Galactic interstellar reddening curve. We test the validity of this assumption by constructing a color-color diagram from our near-IR images, which also provides a check on the extinction measurement indicated by the (V–H) map.

From the (V–H), (J–H)_N, and (H–K)_N color maps, we analyze only pixels lying a distance R from the nucleus such that $0''.25 \leq R \leq 1''.00$. This annulus excludes pixels too close to the nucleus where the PSF is diffraction-limited for F205W, as well as pixels affected by the dust lane passing $1''.5$ north of the nucleus. Thus, this annulus defines a region containing the nuclear dust and its surroundings that are not affected by the dust apparent in our images. Fig. 3a show the histogram of (V–H) inside this aperture. The shaded region represents pixels from the aperture lying along the major axis of the nuclear dust (P.A. = 72°). Since the nuclear dust is roughly axisymmetric within this annulus, we make the simplifying assumption that these points are representative of all dusty regions within the annulus. None of the shaded points lie toward the blue end of the histogram, suggesting that this blue end represents the intrinsic color of the stellar population, and that the rest of the histogram represents this color affected by internal reddening. The weighted average of the shaded region is (V–H) = 3.50, and the weighted average of the two greatest bins in the histogram (which we adopt as the intrinsic color) is (V–H) = 3.08. The color excess is then $E(V-H) = 0.42$, corresponding to $A_V = 0.50$. This assumes the standard Galactic reddening curve (with $R \equiv A_V/E(B-V) = 3.1$) tabulated by Fitzpatrick (1999).

To determine if this assumed reddening curve is appropriate, we construct the (J–H)_N versus (H–K)_N color-color plot for the same aperture (Fig. 3b). The colors in this plot define a band elongated parallel to the reddening vector which we have determined for our three filters from the same Galactic reddening curve adopted above. Thus, our adopted reddening curve is justified. The apparent thickness of this band is dominated by internal photometric error. The larger filled points mark the colors seen along the major axis of the nuclear dust, i.e., the same region emphasized in Fig. 3a. These emphasized points in Fig. 3b are concentrated toward the red end of the band, as are these points concentrated toward the red end of the (V–H) histogram in Fig. 3a. This distribution in Fig. 3b is thus consistent with our suggestion above that the bluer colors represent the intrinsic color of the stellar population, and that the redder colors represent this intrinsic color affected by internal reddening. We measure the intrinsic colors of the stellar population to be (J–H)_N = 1.03 and (H–K)_N = 0.288, while the median of the dust major axis points has (J–H)_N = 1.10 and (H–K)_N = 0.313. The color excesses are $E(J-H)_N = 0.07$ and $E(H-K)_N = 0.025$, corresponding to $A_V = 0.48$. Within the errors this estimate agrees with that from the (V–H) colors.

This measurement of A_V could be underestimated. The intrinsic colors assumed in the analysis above is actually not the intrinsic color of the stellar population if there is a diffuse component of dust in M84. Such a dust component is difficult to detect via broadband imaging, especially if its distribution follows that of the starlight (e.g., Goudfrooij & de Jong 1995). In Paper I (see their Fig. 4), a histogram of (V–I) in the central $14''.5 \times 8''.4$ showed a peak at (V–I) = 1.4. If

this were to be adopted as the intrinsic color to estimate $\langle A_V \rangle$ (the mean extinction inside this region), then the calculated dust mass (e.g., van Dokkum & Franx 1995), from the pixels redder than the peak in that histogram, would be $\approx 1/7$ of the dust mass detected in the far-IR by IRAS (Roberts et al. 1991, scaled to our adopted distance). Alternatively, Paper I adopted $(V-I) = 1.2$ as the intrinsic color, based on the mean for M84's morphological type in Buta & Williams (1995), and the dust mass found agreed with the value based on the far-IR flux. Therefore, the diffuse component of the dust should not be ignored.

Since we need the extinction toward the nucleus, it would be incorrect to calculate it from the total dust mass since this provides the extinction averaged over kpc scales. However, if $E(V-I) = 0.2$ (the difference between the peak $(V-I)$ indicated by Paper I's WFPC2 images and the adopted intrinsic $(V-I)$ based on morphological type) is attributed to a diffuse component, then (based on the Galactic reddening curve) the extinction associated with the putative diffuse dust component is $A_V = 0.38$. Therefore, for the total extinction we adopt $A_V \approx 0.87$.

Does this estimated extinction, which we have derived from regions within the $0''.25 \leq R \leq 1''.00$ annulus, apply to the nucleus as well? This depends on the spatial distribution of the dust. The dust on this scale has the same morphology as the ionized gas disk (Paper I) which we know to be associated with the nucleus (Paper II). Thus, it is likely that the dust on this scale also lies in a disk. Any variation in extinction across the dust would depend on the inclination and thickness of the disk. For example, if the disk is viewed close to face-on or is thin (compared with its diameter), then the extinction toward the nucleus would be significantly less than it would be toward larger radii, since the line of sight toward the nucleus would have less dust. However, results from Paper II suggest that neither of these scenarios is the case. The model fit to the dynamics of the gas disk indicates that the inclination is $75^\circ - 85^\circ$ with respect to the plane of the sky. If the disk is indeed thin, one expects the velocity dispersion in the gas to be small compared with the rotational velocity, yet Paper II's spectra exhibit very broad emission profiles even away from the nucleus (seen best in [S II] $\lambda\lambda 6717, 6731$), whose widths suggest $\sigma_{\text{gas}} \sim 400 \text{ km s}^{-1}$. This is roughly equal to the highest observed rotational velocity (even after deprojection). Therefore, we conclude that the disk thickness is not negligible and that adopting this extinction estimate for the nucleus would not be inappropriate.

3.2. The Nuclear Spectrum

Since the extinction to the nucleus has been estimated, we turn our attention to the STIS spectrum. The long-slit spectrum in Fig. 1 shows strong absorption lines away from the nucleus, including Fe I (5270 Å), the Mg I b lines at 5167 Å, 5172 Å, 5183 Å (which appear blended together because of the finite instrumental resolution and the stellar velocity dispersion), the G band attributed to CH (4300 Å), and Ca II K and H (3933 Å, 3968 Å). The emission lines seen (such as [O II] $\lambda 3727$, $H\beta$, and [O III] $\lambda\lambda 4959, 5007$) are strongly concentrated into a region $0''.28$ across centered on the nucleus. To measure emission line fluxes, as well as the strengths of stellar

absorption lines at the nucleus compared with the strengths of those lines away from the nucleus, we must extract one-dimensional spectra on and off the nucleus.

Fig. 4 shows the extracted spectra. The nuclear spectrum is an optimal extraction (i.e., each row is weighted by its mean counts) of the central $0''.28$ along the slit. To maximize the S/N in the off-nuclear spectrum, we optimally extract two spectra away from the nucleus centered at radius $R = +2''.6$ and $-2''.6$ with size of $4''.8$, and then add them together. The nuclear spectrum reveals several features not detected in the blue spectrum of Ho, Filippenko, & Sargent (1995) from their ground-based spectroscopic survey of a sample of bright galaxies. Given that the emission lines have relatively low equivalent widths (see below) and a compact spatial distribution (Fig. 1), these emission lines would be severely diluted by stellar light in ground-based spectra. The off-nuclear spectrum shows absorption features typical of a stellar population whose light is dominated by K giants, including the broad absorption feature of MgH centered at $\sim 5100 \text{ \AA}$. In contrast, the absorption features are weak in the nuclear spectrum. To determine if this is simply a consequence of the expected higher velocity dispersion σ near the nucleus, we convolve the off-nuclear spectrum in Fig. 4 with a Gaussian broadening function whose width is determined by the difference in quadrature between the values of σ at the nucleus and at the off-nuclear aperture. Unfortunately, no measurements of the stellar kinematics in M84 with sub-arcsecond resolution exist. We adopt $\sigma = 300 \text{ km s}^{-1}$ for the off-nuclear aperture (Davies & Birkinshaw 1988). To estimate σ at the nucleus at our resolution, we adopt the nuclear $\sigma = 600 \pm 37 \text{ km s}^{-1}$ found by Kormendy et al. (1996) in the center of NGC 3115 after scaling to M84 to correct for the differences in galaxy distance and presumed BH mass. This yields an estimate for M84 that $\sigma \approx 370 \text{ km s}^{-1}$ at the nucleus. The off-nuclear spectrum broadened to this estimated velocity dispersion is shown in Fig. 4 as a dotted line. The absorption lines in this spectrum are much stronger than those in the nuclear spectrum, implying that the weakness of the stellar absorption lines at the nucleus is not an artifact of the stellar kinematics. Very weak features are present in the nuclear spectrum at the wavelengths of Mg I b and the G band, but these features are real with only at most 2σ confidence. The nuclear spectrum has a clear absorption feature from MgH near 5100 \AA , while the Ca II K and H (3933 \AA , 3968 \AA) absorption lines are probably not stellar in origin (see below). This exercise suggests that the nuclear continuum (which Fig. 4 shows to be moderately bluer than that in the off-nuclear spectrum) is dominated by a featureless spectrum from an AGN or hot stars. The contribution from cool stars is $\sim 25\%$ at 5200 \AA (from the diminished equivalent width of Mg I b), and is insignificant in the blue where this other continuum component dominates. In §4 we will address the nature of the bluer continuum component using the emission lines and the spectral energy distribution.

The Ca II K and H (3933 \AA , 3968 \AA) absorption lines (Fig. 4) are clearly much narrower in the nuclear spectrum than in the broadened off-nuclear spectrum. The profile widths in the nuclear spectrum are unresolved, indicating that the absorption arises in a dynamically cold region where the velocity dispersion of the absorbing gas is small relative to its rotational velocity. These lines therefore are produced by interstellar absorption in the gas associated with the dust that

extends in front of the nuclear point source. The dust within a projected distance of ≈ 80 pc of the nucleus is likely to be associated with the nucleus, rather than lying in the foreground (see §3.1). Although the extracted spectrum covers $0''.28$ (23 pc) along the slit, we would not expect to see rotational broadening in these line profiles because the absorbing gas is illuminated by a point source. Confirmation that the dust does indeed lie in a disk requires detecting the molecular gas associated with the dust and measuring its kinematics.

We can use the equivalent widths of these Ca II K and H absorption lines in the nuclear spectrum (9.0 Å and 4.5 Å, respectively) for a very rough consistency check on the extinction derived in §3.1. These line profiles show no evidence of saturation, so we estimate the column density of Ca II in the gas phase along the line of sight toward the nucleus (following Spitzer 1978) to be $N(\text{Ca II}) = 9.5 \times 10^{13} \text{ cm}^{-2}$. Unfortunately, the abundance of Ca II in the interstellar medium is not correlated with the gas density of atomic and molecular hydrogen (which is related to the extinction through the gas to dust ratio) because its abundance can be altered significantly by the two competing effects of condensation of Ca II onto dust grains and the destruction of dust grains (e.g., Savage & Mathis 1979). Thus, we cannot directly convert the Ca II column density into a value of A_V . Instead, as a surrogate we can utilize Na I, since its abundance is correlated with that of H I + H₂ (Welsh et al. 1997), and can find the ratio of Na I to Ca II column densities required by our assumed value of A_V and $N(\text{Ca II})$. However, even this is problematic because the STIS red spectrum from Paper II did not cover the Na I D lines. Nevertheless, $A_V \approx 0.87$ and our observed value of $N(\text{Ca II})$ imply that $N(\text{Na I})/N(\text{Ca II}) = 0.1$ assuming the Galactic gas to dust ratio (Savage & Mathis 1979). For the 64 Galactic lines of sight studied by Siluk & Silk (1974), the value of $N(\text{Na I})/N(\text{Ca II})$ ranges from < 0.05 to 90. If the range of abundances in M84's interstellar medium is similar to those in the Galaxy, then $A_V \approx 0.87$ toward the nucleus is not inconsistent with the equivalent widths of the Ca II absorption lines.

Since our main purpose is to determine the ionization mechanism, we need to measure the emission line fluxes for [O II] $\lambda 3727$, [O III] $\lambda 5007$, and H β . These line ratios will then be considered with the fluxes for [O I] $\lambda 6300$, [N II] $\lambda 6583$, and [S II] $\lambda 6717 + \lambda 6731$ relative to H α from the nuclear spectrum in Paper II (see their Fig. 3 for $R = 0''.00$). Since the blue emission lines are seen only within the central $\approx 0''.28$, we are able to place useful constraints on the ionization mechanism only at the nucleus, not at larger radii in the 82 pc diameter gas disk. These emission line ratios clearly distinguish normal H II regions, LINERs, and Seyfert galaxies (e.g., Veilleux & Osterbrock 1987). The emission line ratios of [O III] $\lambda 5007/\text{H}\beta$, [O I] $\lambda 6300/\text{H}\alpha$, [N II] $\lambda 6583/\text{H}\alpha$, and ([S II] $\lambda 6717 + \lambda 6731)/\text{H}\alpha$ are insensitive to uncertainties in the reddening correction, unlike other ratios such as [O II] $\lambda 3727/[\text{O III}] \lambda 5007$. This advantage is particularly important for M84 since our knowledge of the reddening is uncertain. However, a significant disadvantage (which we address in §4) in the use of Balmer emission line fluxes is that their apparent fluxes can be significantly lower than their true fluxes if the stellar light in the aperture has strong Balmer absorption lines, which could arise if there is a significant population of A stars at the nucleus.

Fig. 4b shows the nuclear spectrum corrected for the internal extinction of $A_V = 0.87$ estimated

above. The emission line profiles have a velocity structure more complicated than a Gaussian profile, reflecting the velocity gradient along the slit seen in the emission lines in Fig. 1. Consequently, instead of fitting Gaussian profiles to the emission lines, the continuum flux, line flux, equivalent width, and width of each line, shown in Table 1, were measured directly from the spectrum. We quote the fluxes corrected for Galactic extinction only, as well as fluxes corrected for Galactic and internal extinction. The [O III] profile was deblended by assuming that the ratio of their fluxes $F([\text{O III}] \lambda 4959)/F([\text{O III}] \lambda 5007)$ is 0.335, as given by the ratio of their transition probabilities. The line widths have been corrected for the instrumental width expected for a point source (§2) by assuming that the observed width is the sum in quadrature of the true and instrumental widths.

Measuring emission line fluxes for [O I] $\lambda 6300$, $\text{H}\alpha$, [N II] $\lambda 6583$, and [S II] $\lambda\lambda 6717, 6731$ from Paper II’s spectrum is more uncertain. Even though this spectrum has higher resolution, the line profiles (especially [N II] and $\text{H}\alpha$) are severely blended. Since we could find no clear method to deblend the profiles uniquely, we assume that the peak flux above the continuum level at the central wavelength of each emission line is representative of that emission line’s total flux. Since it is difficult to locate the peak of the [N II] $\lambda 6548$ profile, we assume that $F([\text{N II}] \lambda 6548)/F([\text{N II}] \lambda 6583) = 1/3$, which is the ratio of their transition probabilities. Our assumption that the peak flux is representative of the total flux implies that the velocity structure of each emission line is identical, which might not be strictly true. M84’s nucleus might contain a broad line region, in which case the $\text{H}\alpha$ profile would not be identical to those of the forbidden lines. However, any broad $\text{H}\alpha$ component must be at most a small fraction of the total $\text{H}\alpha$ flux, because a broad $\text{H}\beta$ component is not obvious. Also, the forbidden lines might have different velocity widths, since their critical densities for collisional de-excitation are different. Correlations between line width and critical density have been found in Seyfert galaxies (e.g., De Robertis & Osterbrock 1984, 1986) and LINERs (e.g., Filippenko & Halpern 1984). Table 2 lists our measured line fluxes relative to $\text{H}\alpha$, separately corrected for Galactic reddening only, as well as Galactic and internal reddening. The errors in these fluxes reflect the fact that the observed line profiles cannot be decomposed uniquely, and are dominated by the uncertainty in our assumption that the velocity structure in each component is identical. We conservatively adopt errors of 50% for [N II] $\lambda 6583/\text{H}\alpha$ and 25% for [O I] $\lambda 6300/\text{H}\alpha$ and ([S II] $\lambda 6717 + \lambda 6731)/\text{H}\alpha$. We have much more confidence in the [O I] and [S II] relative fluxes compared with the [N II] relative flux because these lines are not blended with any other emission lines, so only the uncertainty in $\text{H}\alpha$ is present for these two line ratios.

4. Interpretation

The goal of this section is to determine the constraints that can be placed on the nuclear emission mechanism from the nuclear emission line ratios and spectral energy distribution. The emission line ratios (discussed in §4.2) include the fluxes in Balmer emission lines measured in §3.2. These fluxes might be underestimated if there is significant Balmer absorption arising from the stellar population at the nucleus. If significant, such absorption lines could cause an underestimate

of the $H\alpha$ and $H\beta$ emission line flux, leading to a misclassification of the emission line spectrum. We consider this possibility in §4.1.

4.1. The Insignificance of Balmer Absorption Features

In order to use the line fluxes as a diagnostic of the ionization mechanism at the nucleus, we must determine the significance of Balmer absorption lines in the nuclear spectrum. Although the nuclear spectrum in Fig. 4b shows that $H\beta$ and $H\gamma$ are in emission, the nebular emission component for higher Balmer transitions is not observed. We would expect the higher transitions to appear in absorption, if A stars are significant. However, the [S II] $\lambda\lambda 4069, 4076$ emission dilutes any $H\delta$ $\lambda 4101$ absorption, and the Ca II H $\lambda 3968$ absorption from the dust disk masks any $H\epsilon$ $\lambda 3970$ absorption. Even higher Balmer transitions have lower equivalent widths in A stars, rendering their detection more difficult. The best spectral feature in A stars remaining is the prominent Balmer absorption edge at 3646 \AA . Although the nuclear spectrum in Fig. 4b shows no evidence of a Balmer absorption edge, the S/N in the continuum at the wavelength of this absorption edge is only 10 pixel^{-1} . It could be that a Balmer absorption edge is indeed present, but is significantly diluted by a featureless continuum that may be emitted by the nucleus. We construct synthetic spectra and compare them with the data to place an upper limit on the possible contribution of Balmer absorption lines (primarily from A stars).

Our synthetic spectra are simply linear combinations of an A0 V spectrum from the library of Pickles (1998) with a power law spectrum. The A0 V spectrum has a resolution of 5 \AA (which is very close to our resolution) and has solar metallicity. The power law component adopted has $F_\lambda \propto \lambda^\beta$ (where $\beta = 4.33$ is a good approximation of the shape of the continuum in the nuclear spectrum at $\lambda \leq 5000 \text{ \AA}$ (Fig. 4b)). We adopt an A0 V spectrum as a proxy for a hypothetical nuclear cluster of young stars in favor of a more complicated approach involving synthetic starburst spectra (e.g., Bruzual & Charlot 1993; Leitherer & Heckman 1995), because starburst models involve several parameters which would be very poorly constrained in this case. This includes the star formation history (i.e., an instantaneous starburst or a constant star formation rate), age, initial mass function, and metallicity. In utilizing more sophisticated starburst models, it would be very difficult to translate the observed lack of a Balmer absorption edge in M84's nucleus to a meaningful limit on possible Balmer absorption line equivalent width.

Fig. 5 shows the input A0 V and power law spectra, where both have been normalized to unit flux at 5556 \AA , and the synthetic spectra constructed from a linear combination of these two input spectra with Gaussian noise added to simulate the observed nuclear continuum component from Fig. 4b. The fit to the continuum of the observed spectrum is superimposed for comparison. If A stars represent at least 15% of the light in the nuclear point source, then we should have detected a Balmer absorption edge. We conclude that A0 V stars contribute at most 10% of the total light in the blue nuclear spectrum, and the equivalent width (EW) of Balmer absorption features are at most 10% of the strengths in an A0 V star, for which Pickles (1998) finds $H\beta$ and $H\alpha$ equivalent

widths to be 13.4 Å and 9.8 Å, respectively. This implies that the upper limits to absorption lines are $EW(H\beta) < 1.4 \text{ \AA}$ and $EW(H\alpha) < 1.0 \text{ \AA}$.

Given the continuum flux near $H\beta$ corrected for internal extinction listed in Table 1, this upper limit on $H\beta$ absorption could hide an emission line flux of $< 3.8 \times 10^{-16} \text{ erg cm}^{-2} \text{ s}^{-1}$, so the $H\beta$ flux, corrected for possible underlying stellar absorption, is at most $2.49 \times 10^{-15} \text{ erg cm}^{-2} \text{ s}^{-1}$, or at most 18% above the observed flux. For the correction of $H\alpha$, the equivalent width of the $H\alpha + [N \text{ II}]$ profile in Paper II's spectrum is 274 Å. Table 2 indicates that the $H\alpha$ flux is 38% of the $H\alpha + [N \text{ II}]$ flux, so $EW(H\alpha)$ is approximately 105 Å. Any correction for possible stellar absorption (which is at most 1%) is much smaller than the uncertainty in the $H\alpha$ flux arising through the uncertainty in emission line deblending. Consequently, we ignore this correction.

4.2. Emission Line Diagnostics of the Ionizing Continuum

Fig. 6 shows the emission line ratios in the diagnostic diagrams from Veilleux & Osterbrock (1987), which are insensitive to uncertainties in the reddening correction, as well as the $[O \text{ II}] \lambda 3727/[O \text{ III}] \lambda 5007$ diagram (e.g., Shields & Filippenko 1990). The point representing M84's nucleus is clearly segregated from the regime of normal H II regions. It is also not consistent with the H II region models of Filippenko & Terlevich (1992) in which O stars photoionize solar metallicity nebular gas and the ionization parameter is low ($\log U \approx -3.7$ to -3). Their Fig. 1 shows that these models produce LINER spectra with lower excitation than we find in M84's nucleus, as indicated by the value of $[O \text{ III}] \lambda 5007/H\beta$. Our measurements indicate that hot stars play at most a very minor role in the ionization mechanism at the nucleus. This would be consistent with our determination that A stars do not significantly contribute to the spectrum of the nucleus, if the IMF of the stellar population associated with the nucleus is roughly similar to a Salpeter function. In the emission line ratio diagrams, for convenience we have adopted lines that separate the loci of Seyfert galaxies and LINERs given by $[O \text{ III}] \lambda 5007/H\beta = 3$ and $[O \text{ II}] \lambda 3727/[O \text{ III}] \lambda 5007 = 1$. M84's nuclear line ratios are very close to these lines in all four plots, so its classification between these two types is ambiguous. However, exact divisions between these two types are somewhat arbitrary. We compare the position of M84 in these plots to that of M87 [whose nuclear and off-nuclear line ratios are taken from Chakrabarti (1995) and Dopita et al. (1997)], since these two galaxies have many features in common. Both are radio galaxies containing nuclear gas disks (with diameters $\sim 100 \text{ pc}$). In each case, the gas disk has a Keplerian velocity field (Paper II; Macchetto et al. 1997), indicating the presence of a $\sim 10^9 M_\odot$ dark compact object, which presumably is in the form of a black hole. M84's nucleus clearly has significantly higher excitation than most LINERs, including M87. It is more consistent with the higher excitation found in Seyfert nuclei. The $[O \text{ II}] \lambda 3727/[O \text{ III}] \lambda 5007$ ratio, which is sensitive to the assumed reddening correction, is marginally more consistent with the classification derived from the other line ratios shown (which are insensitive to reddening) if there is no correction for internal reddening at all. Perhaps the amount of dust within a few pc of the nucleus is lower than it is at larger radii in the dust disk,

contrary to our expectation given in §3.1. However, the extinction to the nucleus cannot be zero, since Ca II absorption lines from the ISM are seen against the background nuclear point source.

4.3. The Ionizing Photon Flux from the Nuclear Source

Since the ionization conditions in M84’s nucleus are more consistent with Seyfert nuclei than LINERs, the ionization mechanism is probably photoionization from either the AGN or perhaps high-velocity shocks [which can generate a strong UV radiation field capable of ionizing the gas, resulting in a high-excitation emission line spectrum (e.g., Allen et al. 1998)]. The ionizing flux required can be estimated by assuming case B recombination (i.e., the gas is optically thick to Lyman continuum photons) and that the electron temperature in the ionized gas is 10^4 K. The ionizing luminosity $Q(\text{H}^0)$ is then related to the $\text{H}\beta$ luminosity (Osterbrock 1989). The $\text{H}\beta$ flux from Table 1 corresponds to a luminosity $L(\text{H}\beta)$ of 2.9×10^{37} erg s^{-1} (corrected for Galactic extinction but not internal extinction) or 7.4×10^{37} erg s^{-1} (corrected for both Galactic and internal extinction). We calculate that the ionizing luminosity is $Q(\text{H}^0) \approx 1.5 \times 10^{50}$ photons s^{-1} . This is a lower limit if the nebular gas close to the nucleus (within the volume spatially unresolved in the spectrum) has a clumpy distribution so that some ionizing photons can escape without being reprocessed by the gas.

4.4. The Spectral Energy Distribution of the Nuclear Source

The spectral energy distribution (SED) of the nonstellar point source in the nucleus of M84 is important because knowledge of the SEDs in low luminosity AGN should provide key insights into the physics of these objects. However, the measurement of fluxes from low luminosity AGN is complicated by the need for both high sensitivity and spatial resolution, to distinguish the faint AGN from its host galaxy. Ho (1999) compiled such data from the literature for a sample of seven low luminosity AGN including M84. This preliminary SED for M84 can be improved significantly through the addition of measurements from our new HST data and from archival Infrared Satellite Observatory (ISO) images.

Our STIS spectrum provides a clear detection of the nuclear point source extending blueward of the V band, a region for which no detections existed previously in its SED (Ho 1999). To determine if the nuclear source is variable, in Table 3 we list the nuclear V band magnitudes (corrected for Galactic extinction) determined from our STIS spectrum (Fig. 4a) and the two epochs of HST V band images. For the two HST V band images, we isolate the nuclear flux from the host galaxy by fitting model PSFs (Krist & Hook 1997) to the nucleus (as in Paper I). From our STIS spectrum, we extract the intensity profile along the slit (perpendicular to the dispersion axis) using a bandpass whose wavelength coverage matches the filter bandpasses of the HST V band images. We then repeat the PSF fitting (albeit with one spatial dimension instead of two) to isolate the nuclear flux

from the host galaxy, finding that the observed flux at the V band is $5.1 \times 10^{-17} \text{ erg cm}^{-2} \text{ s}^{-1} \text{ \AA}^{-1}$. The error on these magnitudes of the nuclear source is no larger than 0.1 mag, which is dominated by the uncertainty in isolating the nucleus from the host galaxy. We list the nuclear magnitudes from these three epochs in Table 3. During this time, the nucleus has brightened in V band by $\approx 75\%$, adding more confidence to our result that the nucleus is nonstellar.

To measure the flux from the nuclear point source in the NICMOS images in Fig. 2, first we subtract the host galaxy using a fit to the surface brightness distribution beyond $0''.6$ from the nucleus. This restriction is required to avoid emission from the nuclear point source within the first diffraction ring. The fit was extrapolated inward from this distance toward the nucleus. Since the stellar surface brightness profile is very shallow within its break radius of $2''.45$ (Quillen et al. 1999), this extrapolation is insensitive to the details of the fit. Subtracting this model for the host galaxy from the original image isolates the nuclear point source. We then measured the flux of this source using aperture corrections derived from a model PSF generated with Tiny Tim (Krist & Hook 1997). Our measured fluxes are 0.22 mJy (F110W), 0.41 mJy (F160W), and 0.42 mJy (F205W).

The SED can be extended into the mid-infrared using observations by ISO¹⁰ (Kessler et al. 1996) with ISOCAM (Cesarsky et al. 1996) obtained by F. Macchetto on 5 July 1996. The images were obtained in the three bandpasses LW2 ($6.75 \mu\text{m}$), LW7 ($9.62 \mu\text{m}$), and LW3 ($15 \mu\text{m}$) in the $3''/\text{pixel}$ mode (spatial resolution $\approx 5'' - 8''$). We retrieved these images from the ISO archive and then resampled the WFPC2 F547M image, after subtracting the nuclear point source, to match the plate scale and resolution of each of the three ISOCAM images. No significant difference was found between the light profiles in this resampled WFPC2 image (which provides the stellar light distribution) and the ISOCAM images, implying that the mid-infrared emission is associated with the stars and that the nuclear point source was not detected at these mid-infrared wavelengths. For each ISOCAM image, we estimated an upper limit on the flux from this nuclear source (detected in the WFPC2 and NICMOS images) from twice the flux of the brightest ISOCAM pixel (minus the background). These upper limits are $< 10 \text{ mJy}$ (LW2), $< 6 \text{ mJy}$ (LW7), and $< 5 \text{ mJy}$ (LW3).

Table 4 compiles these new flux measurements with the previous measurements from Ho (1999) that have not been superseded by new results. We note that Ho (1999) misquoted the 2300 \AA upper limit found by Zirbel & Baum (1998). This updated SED is shown in Fig. 7 along with our spectrum of the nucleus from Fig. 4b. We note the caveat that the observations composing this SED are obviously not simultaneous, and the source is variable at least at optical wavelengths (see above). As noted in §3.2, the contribution of host galaxy starlight to the nuclear spectrum is $\sim 25\%$ of the total light at 5200 \AA but is negligible at shorter wavelengths. We superimpose the mean SED of radio loud quasars (Elvis et al. 1994) and the SED of BL Lac (Bregman et al. 1990), both normalized to M84 at K band. More recent compilations of the SEDs of BL Lac objects in the literature do not have sufficient frequency resolution to compare them adequately with M84. We do

¹⁰The Infrared Space Observatory (ISO) is an ESA (European Space Agency) mission with the participation of ISAS (Japan) and NASA (USA).

not overplot the mean SED of Seyfert 2 nuclei (e.g., Schmitt et al. 1997) because it is approximately two orders of magnitude too faint at radio frequencies. M84’s SED is significantly different from the mean radio loud quasar SED at the wavelength range covered by our spectrum. At blue and near-UV wavelengths, M84’s SED is very red, whereas the mean radio loud quasar SED has the big blue bump. M84’s SED is more similar to that of BL Lac. This normalization of BL Lac’s SED has an ionizing luminosity of $Q(\text{H}^0) = 1.4 \times 10^{50} \text{ erg s}^{-1}$. This is only 7% lower than the lower limit on $Q(\text{H}^0)$ for M84’s nucleus estimated from the $\text{H}\beta$ luminosity in §4.3, suggesting that the SEDs of M84’s nucleus and BL Lac could very well be similar at energies greater than 13.6 eV ($3.28 \times 10^{15} \text{ Hz}$). Since our M84 SED has sparse frequency coverage, we use the normalized BL Lac SED shown in Fig. 7 as a template to estimate that the bolometric luminosity of M84’s nuclear point source is $\sim 1 \times 10^{41} \text{ erg s}^{-1}$, assuming isotropic emission. However, as a cautionary note, this could be significantly underestimated if the nuclear emission is beamed away from us (see §5). Since the mass of the compact dark object (most likely a BH) is $\approx 1.5 \times 10^9 M_\odot$ (Paper II), this estimated bolometric luminosity is only $\sim 5 \times 10^{-7}$ of the Eddington luminosity, implying that the BH in M84 is accreting at a very low rate.

5. Conclusion

The following four implications of our observations show that the nuclear point source in M84 cannot be a star cluster:

1. Stellar absorption lines at the nucleus are very weak. Cool stars make a minor contribution to the total light.
2. A Balmer absorption edge is not detected. Thus, the contribution of A stars is insignificant.
3. The emission line ratios indicate that the gas is not photoionized by hot stars. Therefore, OB stars are insignificant as well.
4. The spectral energy distribution (SED) of the nuclear source is also strong evidence that it is nonstellar. We have updated the preliminary SED compiled by Ho (1999). This updated SED is roughly flat, which is vastly different from the SED of a stellar cluster. Among types of AGN, the SED of M84’s nucleus is more similar to the SED of BL Lac than that of radio loud quasars. Specifically, M84’s nucleus is characterized by a very red continuum at optical to UV wavelengths where radio loud quasars have very blue continua. We have adopted the SED of BL Lac as a template to estimate the bolometric luminosity of M84’s nuclear source assuming isotropic emission, implying that the luminosity is only $\sim 5 \times 10^{-7}$ of the Eddington luminosity.

The similarity between the SEDs of M84’s nuclear source and BL Lac plus its V band variability suggest the possibility that M84 might be a misaligned BL Lac object. In that case, our assumption of isotropic emission, for the purpose of estimating the bolometric luminosity, would be invalid since the radiation could be beamed away from us. The characteristics of M84’s radio source imply that

this possibility should be investigated further. Its radio jets are nearly in the plane of the sky (as indicated by the roughly comparable power in the radio jets and lobes on either side of the nucleus; Laing & Bridle 1987). Is the optical emission beamed in the same manner? If so, then the evidence for M84 being a misaligned BL Lac object would be strengthened. This would fit with the evidence suggesting that BL Lac objects are a subset of FR I radio galaxies that are oriented such that their jets are beamed directly at us (e.g., Urry & Padovani 1995). In that case, it is interesting that Centaurus A and M87 (two other nearby FR I radio galaxies) also show evidence of being misaligned BL Lac objects. For Centaurus A where direct observation of the nucleus is not possible at optical and UV wavelengths, Morganti et al. (1991, 1992) found that the ionization conditions in gaseous filaments ~ 9 kpc northeast of the nucleus suggest that this gas is photoionized by beamed radiation from the nucleus. However, the shock models constructed by Sutherland, Bicknell, & Dopita (1993) suggest that the ionization source of these clouds could arise from the interaction between the radio jet and the galaxy’s ISM. For M87, the evidence of a misaligned BL Lac is indicated by its variability characteristics at optical wavelengths (Tsvetanov et al. 1998), the detection of superluminal motion in its relativistically boosted jet (Biretta, Zhou, & Owen 1995; Biretta, Sparks, & Macchetto 1999), and its radio to optical and optical to X-ray spectral indices (Biretta, Stern, & Harris 1991; Boksenberg et al. 1992).

We thank the referee for several useful suggestions. This work was supported by NASA Guaranteed Time Observer funding to the STIS Science Team and by funding from NASA through grant number GO-07868.01-96A (to ACQ) from the Space Telescope Science Institute, which is operated by AURA, Inc., under NASA contract NAS5-26555.

References

- Allen, M. G., Dopita, M. A., & Tsvetanov, Z. I. 1998, ApJ, 493, 571
- Biretta, J. A., Sparks, W. B., & Macchetto, F. 1999, ApJ, 520, 621
- Biretta, J. A., Stern, C. P., & Harris, D. E. 1991, AJ, 101, 1632
- Biretta, J. A., Zhou, F., & Owen, F. N. 1995, ApJ, 447, 582
- Boksenberg, A., et al. 1992, A&A, 261, 393
- Bower, G. A., Heckman, T. M., Wilson, A. S., & Richstone, D. O. 1997, ApJ, 483, L33
(Paper I)
- Bower, G. A., et al. 1998, ApJ, 492, L111 (Paper II)
- Bregman, J. N., et al. 1990, ApJ, 352, 574
- Bruzual, G. A., & Charlot, S. 1993, ApJ, 405, 538
- Burstein, D., & Heiles, C. 1984, ApJS, 54, 33
- Buta, R., & Williams, K. L. 1995, AJ, 109, 543
- Cesarsky, C. J., et al. 1996, A&A, 315, L32
- Chakrabarti, S. K. 1995, ApJ, 441, 576
- Davies, R. L., & Birkinshaw, M. 1988, ApJS, 68, 409
- De Robertis, M. M., & Osterbrock, D. E. 1984, ApJ, 286, 171
- De Robertis, M. M., & Osterbrock, D. E. 1986, ApJ, 301, 727
- Dopita, M. A., et al. 1997, ApJ, 490, 202
- Elvis, M., et al. 1994, ApJS, 95, 1
- Fabbiano, G., Kim, D.-W., & Trinchieri, G. 1992, ApJS, 80, 531
- Faber, S. M., et al. 1997, AJ, 114, 1771
- Filippenko, A. V., & Halpern, J. P. 1984, ApJ, 285, 458
- Filippenko, A. V., & Terlevich, R. 1992, ApJ, 397, L79
- Fitzpatrick, E. L. 1999, PASP, 111, 63
- Goudfrooij, P., & de Jong, T. 1995, A&A, 298, 784
- Harms, R. J., et al. 1994, ApJ, 435, L35
- Ho, L. C. 1999, ApJ, 516, 672
- Ho, L. C., Filippenko, A. V., & Sargent, W. L. W. 1995, ApJS, 98, 477
- Jaffe, W., Ford, H. C., O'Connell, R. W., van den Bosch, F. C., & Ferrarese, L. 1994, AJ,
108, 1567
- Jones, D. L., Terzian, Y., & Sramek, R. A. 1981, ApJ, 246, 28
- Kessler, M. F., et al. 1996, A&A, 315, L27
- Kimble, R. A., et al. 1998, ApJ, 492, L83
- Kormendy, J., et al. 1996, ApJ, 459, L57
- Krist, J., & Hook, R. 1997, The Tiny Tim User's Guide, <http://scivax.stsci.edu/~krist/tinytim.html>
- Laing, R. A., & Bridle, A. H. 1987, MNRAS, 228, 557
- Leitherer, C., & Heckman, T. M. 1995, ApJS, 96, 9
- Macchetto, F., et al. 1997, ApJ, 489, 579
- MacKenty, J. W., et al. 1997, NICMOS Instrument Handbook, Version 2.0 (Baltimore:

STScI)

- Maoz, D., et al. 1998, *AJ*, 116, 55
- Morganti, R., et al. 1991, *MNRAS*, 249, 91
- Morganti, R., Fosbury, R. A. E., Hook, R. N., Robinson, A., & Tsvetanov, Z. 1992, *MNRAS*, 256, P1
- Mould, J., et al. 1995, *ApJ*, 449, 413
- Osterbrock, D. E. 1989, *Astrophysics of Gaseous Nebulae and Active Galactic Nuclei* (Mill Valley, CA: University Science Books)
- Pickles, A. J. 1998, *PASP*, 110, 863
- Quillen, A. C., Bower, G. A., & Stritzinger, M. 1999, *ApJS*, in press (astro-ph/9907021)
- Richstone, D., et al. 1998, *Nature*, 395, A14
- Roberts, M. S., Hogg, D. E., Bregman, J. N., Forman, W. R., & Jones, C. 1991, *ApJS*, 75, 751
- Savage, B. D., & Mathis, J. S. 1979, *ARA&A* 17, 73
- Schilizzi, R. T. 1976, *AJ*, 81, 946
- Schmitt, H. R., Kinney, A. L., Calzetti, D., & Storchi-Bergmann, T. 1997, *AJ*, 114, 592
- Shields, J. C., & Filippenko, A. V. 1990, *AJ*, 100, 1034
- Siluk, R. S., & Silk, J. 1974, *ApJ*, 192, 51
- Spitzer, L. 1978, *Physical Processes in the Interstellar Medium* (New York: Wiley)
- Sutherland, R. S., Bicknell, G. V., & Dopita, M. A. 1993, *ApJ*, 414, 510
- Thompson, R. I., Rieke, M., Schneider, G., Hines, D. C., & Corbin, M. R. 1998, *ApJ*, 492, L95
- Tsvetanov, Z. I., et al. 1998, *ApJ*, 493, L83
- Urry, C. M., & Padovani, P. 1995, *PASP*, 107, 803
- van Dokkum, P. G., & Franx, M. 1995, *AJ*, 110, 2027
- Veilleux, S., & Osterbrock, D. E. 1987, *ApJS*, 63, 295
- Walborn, N., & Baum, S. (ed) 1998, *STIS Instrument Handbook, Version 2.0* (Baltimore: STScI)
- Welsh, B. Y., Sasseen, T., Craig, N., Jelinsky, S., & Albert, C. E. 1997, *ApJS*, 112, 507
- Woodgate, B. E., et al. 1998, *PASP*, 110, 1183
- Zirbel, E. L., & Baum, S. A. 1998, *ApJS*, 114, 177

Fig. 1.— The reduced two-dimensional spectrum of M84. The wavelength scale is in the observer’s reference frame. The radius scale is defined such that $R = 0$ corresponds to the position of the nucleus, and positive radii correspond to the direction along the slit with P.A. = 130° on the sky. The dynamic range of the linear intensity scale covers -1.0 (white) to ≥ 3.0 (black) in units of $10^{-17} \text{ erg cm}^{-2} \text{ s}^{-1} \text{ \AA}^{-1}$.

Fig. 2.— The WFPC2 image (taken from Paper I) and NICMOS images of the nuclear region of M84. All images have identical field of view and orientation (north is up, and east to the left), with the nucleus at the origin of the coordinate system. The top four panels show the images in the indicated bandpasses (the intensity stretch is logarithmic). The displayed intensity ranges and peak intensities (in units of $\text{erg cm}^{-2} \text{ s}^{-1} \text{ \AA}^{-1} \text{ arcsec}^{-2}$) for the WFPC2/F547M image are: 2.4×10^{-16} to 2.4×10^{-15} , and 3.1×10^{-15} , respectively. The displayed intensity range for all three NICMOS images is $1.24 \text{ mJy arcsec}^{-2}$ to $12.4 \text{ mJy arcsec}^{-2}$, and their peak intensities in these units are 9.4 (F110W), 13.7 (F160W), and 12.3 (F205W). The lower two panels show $(J-H)_N$ and $(H-K)_N$. The displayed color values range linearly from $(J-H)_N$ of 1.18 to 0.99 and $(H-K)_N$ of 0.42 to 0.19. Darker shades correspond to redder colors. Since the PSF through the F205W filter is different from that through F110W and F160W, the apparent $(H-K)_N$ within $0''.25$ of the nuclear point source should be disregarded (see §3.1).

Fig. 3.— Analysis of the colors (corrected for foreground Galactic reddening) inside an annular aperture centered on the nucleus (see §3.1). (a) The distribution of $(V-H)$. The shaded region represents pixels lying in the major axis of the nuclear dust lane. (b) The $(J-H)_N$ versus $(H-K)_N$ color-color plot. The larger filled circles represent pixels lying in the major axis of the nuclear dust lane. The open boxes represent the median of these twenty points and the adopted color unreddened by dust apparent in the broadband images. The open circle shows the color in an aperture with radius of $0''.25$ centered on the nucleus.

Fig. 4.— (a) Extracted spectra (solid lines) of the nuclear point source and the off-nucleus stellar light. The flux scale on the left is in units of $10^{-15} \text{ erg cm}^{-2} \text{ s}^{-1} \text{ \AA}^{-1}$. The one on the right is normalized by the mean flux in the wavelength interval displayed. Both spectra are displayed on the same normalized flux scale. The wavelength scale λ_0 shows vacuum wavelength in the rest frame. The dotted line represents the off-nuclear spectrum broadened to match the adopted velocity dispersion at the nucleus. This spectrum is shifted downward by 1.6 normalized flux units. (b) The spectrum of the nuclear point source from (a) corrected for Galactic and internal extinction. A fit to the continuum (a sixth order polynomial) is shown as a dashed line.

Fig. 5.— (a) The input spectra from which the synthetic spectra are constructed. Both the A0 V and power-law nonstellar spectra are normalized to unit flux at 5556 \AA . (b) The synthetic spectra constructed from a linear combination of the input spectra in (a) with Gaussian noise added. Each spectrum is labeled with the fraction of the light originating from A stars. The flux scale on the left applies to the spectrum where 10% of the light originates from A stars. The others are shifted vertically for clarity. The fit to the continuum of the observed spectrum (Fig. 4b) is superimposed

for comparison.

Fig. 6.— The emission line ratios of M84’s nucleus. The closed circles represent the line fluxes from Tables 1 and 2 corrected for both Galactic and internal reddening. For line ratios involving $H\beta$, the open circle would be the position of M84 if the correction for $H\beta$ absorption is equal to the upper limit derived in the text. The true position of M84 must be between these two points. For the $[O\ II]\ \lambda 3727/[O\ III]\ \lambda 5007$ plot, the flux ratio from Table 1 corrected only for Galactic extinction is represented by the open diamond. M87 is represented by closed and open triangles. The closed triangle shows the average emission line ratios in the central $0''.78 = 64\text{ pc}$ (Chakrabarti 1995, from the spectra of Harms et al. 1994), while the open triangle represents the emission line ratios at $0''.6$ (49 pc) from the nucleus along the major axis of its gas disk (Dopita et al. 1997). The error bars claimed for M87 are not much larger than the size of the points.

Fig. 7.— The spectral energy distribution (SED) of M84’s nuclear point source (filled points and upper limits), including our nuclear spectrum (short solid line) from Fig. 4b after it was convolved with a median filter 11 pixels wide (to emphasize the continuum shape). The dotted line represents the mean SED of radio loud quasars (Elvis et al. 1994). The small open circles represent the SED of BL Lac (Bregman et al. 1990); these points are connected by the dashed line. Both the radio loud quasar and BL Lac SEDs have been normalized to M84’s SED at K band. We use the dashed line to estimate the bolometric luminosity of M84’s nuclear point source in the text.

Table 1. Emission Line Fluxes for the Nuclear Spectrum

Emission Line	F_{Cont}^G	F^G	$F_{Cont}^{G,i}$	$F^{G,i}$	EW (Å)	FWHM (km s ⁻¹)
[O II] λ3727	0.37 ± 0.09	2.93 ± 0.33	1.20 ± 0.32	9.44 ± 1.08	78 ± 8	1325
[Ne III] λ3869	0.44 ± 0.08	0.24 ± 0.18	1.37 ± 0.27	0.76 ± 0.57	5 ± 4	756
[S II] λλ4069, 4076	0.69 ± 0.04	1.05 ± 0.33	2.08 ± 0.13	3.15 ± 0.99	15 ± 4	2625
Hβ λ4861	1.10 ± 0.03	0.85 ± 0.14	2.73 ± 0.08	2.11 ± 0.35	7 ± 1	1299
[O III] λ4959	1.12 ± 0.02	1.14 ± 0.17	2.73 ± 0.07	2.78 ± 0.42	10 ± 1	...
[O III] λ5007	1.14 ± 0.02	3.48 ± 0.17	2.73 ± 0.07	8.31 ± 0.42	30 ± 1	1662

Note. — F_{Cont}^G and $F_{Cont}^{G,i}$ are the continuum fluxes in units of 10^{-16} erg cm⁻² s⁻¹ Å⁻¹ corrected respectively for Galactic extinction, and Galactic plus internal extinction. F^G and $F^{G,i}$ are the emission line fluxes in units of 10^{-15} erg cm⁻² s⁻¹ corrected respectively for Galactic extinction, and Galactic plus internal extinction. EW is the equivalent width.

Table 2. Relative Emission Line Fluxes

Emission Line	F^G	$F^{G,i}$
[O I] λ 6300	0.12	0.13
[N II] λ 6548	0.42	0.43
H α	1.00	1.00
[N II] λ 6583	1.29	1.29
[S II] λ 6717	0.51	0.50
[S II] λ 6731	0.58	0.57

Note. — F^G and $F^{G,i}$ are the relative fluxes corrected respectively for Galactic extinction, and Galactic plus internal extinction.

Table 3. HST V Band Magnitudes for M84’s Nuclear Point Source

Date	HST mode	Spectral Element	λ_{eff} (Å)	$\Delta\lambda$ (Å)	V^a (mag)	Reference
06 Mar 1993	WFPC	F555W	5454	509	20.2	1
04 Mar 1996	WFPC2	F547M	5454	486	19.9	2
10 Apr 1998	STIS/ACCUM	G430L	5454	497	19.6	3

^aCorrected for Galactic extinction but not internal extinction.

References. — (1) Jaffe et al. 1994. (2) Paper I. (3) This paper.

Table 4. The SED of M84’s Nuclear Point Source

ν (Hz)	F_{ν}^a (erg cm ⁻² s ⁻¹ Hz ⁻¹)	Reference
1.67×10^9	1.60×10^{-24}	1
8.09×10^9	1.90×10^{-24}	2
2.00×10^{13}	$< 5.00 \times 10^{-26}$	3
3.11×10^{13}	$< 6.08 \times 10^{-26}$	3
4.44×10^{13}	$< 1.02 \times 10^{-25}$	3
1.46×10^{14}	4.66×10^{-27}	3
1.87×10^{14}	4.76×10^{-27}	3
2.72×10^{14}	2.89×10^{-27}	3
3.63×10^{14}	1.36×10^{-27}	4
5.50×10^{14}	8.83×10^{-28}	4
1.30×10^{15}	$< 9.55 \times 10^{-28}$	5
4.84×10^{17}	$< 1.84 \times 10^{-30}$	6

^aCorrected for Galactic and internal extinction (total $A_V = 0.94$).

References. — (1) Jones et al. 1981. (2) Schilizzi 1976. (3) This paper. (4) Paper I. (5) Zirbel & Baum 1998. (6) Fabbiano et al. 1992.

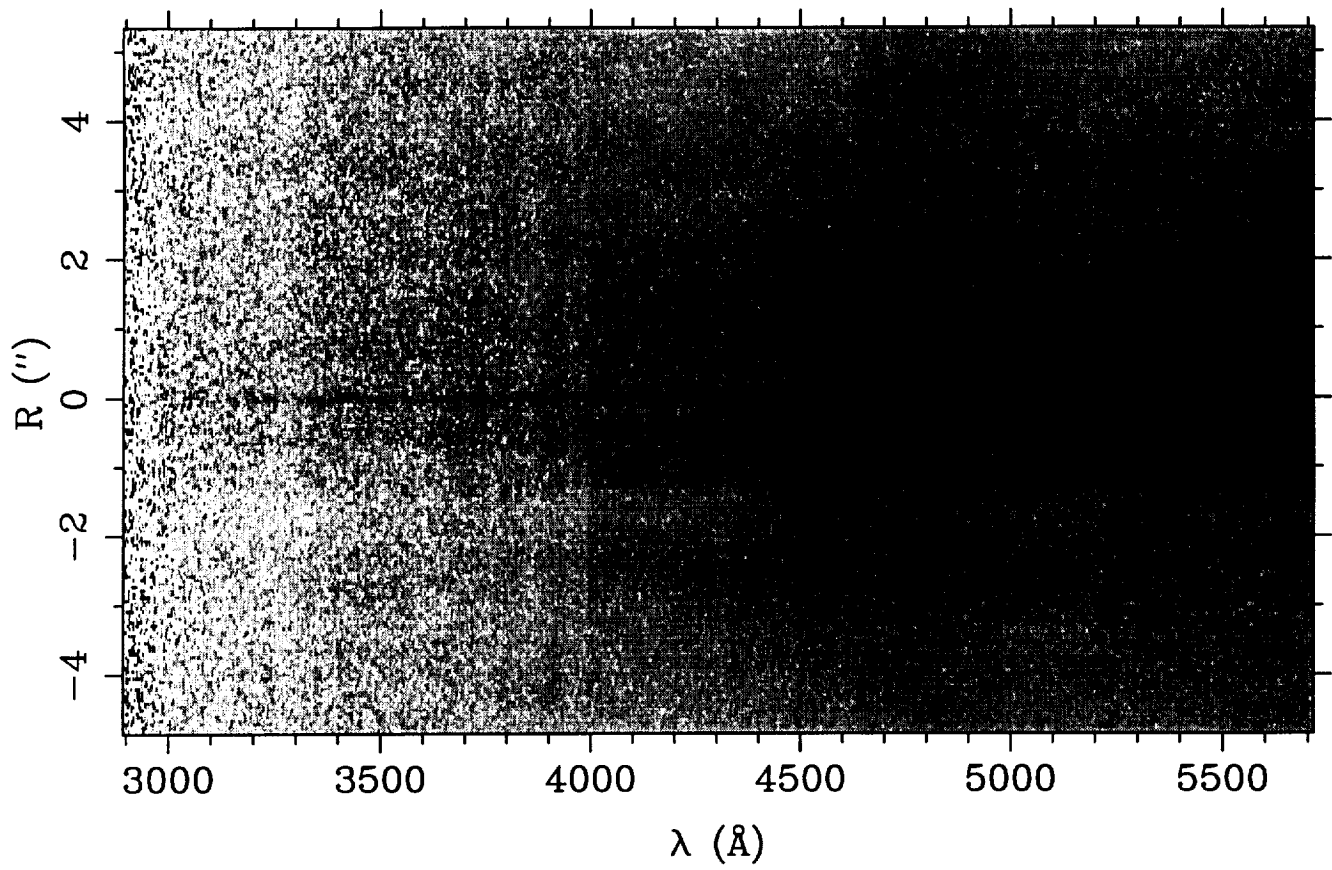
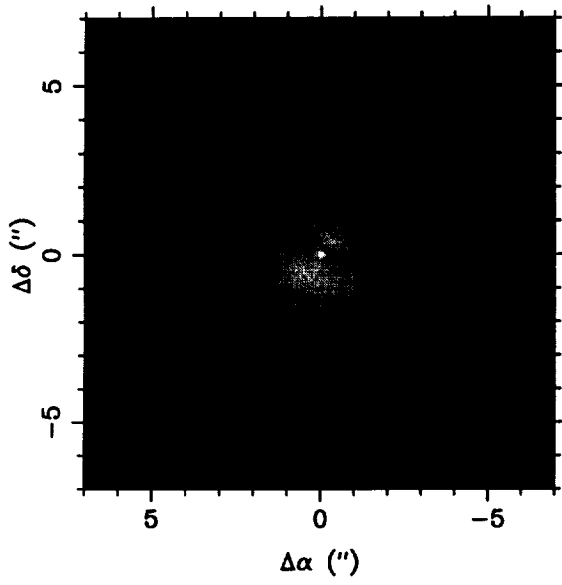
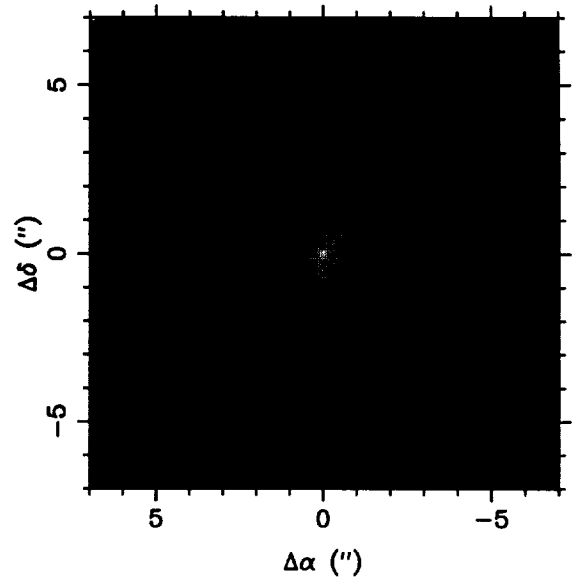


Fig. 1

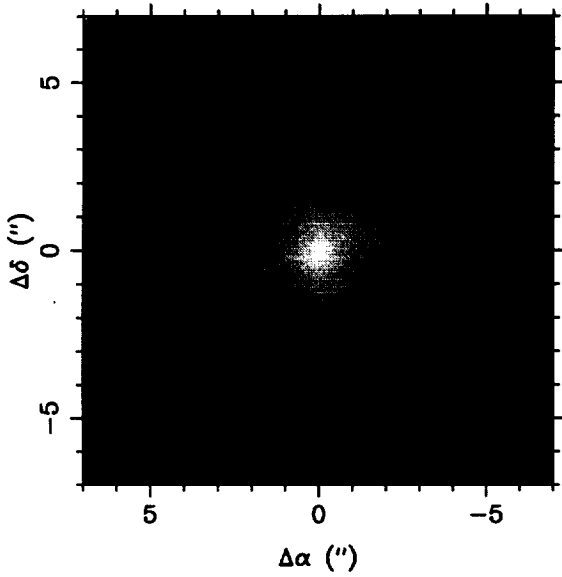
WFPC2/F547M



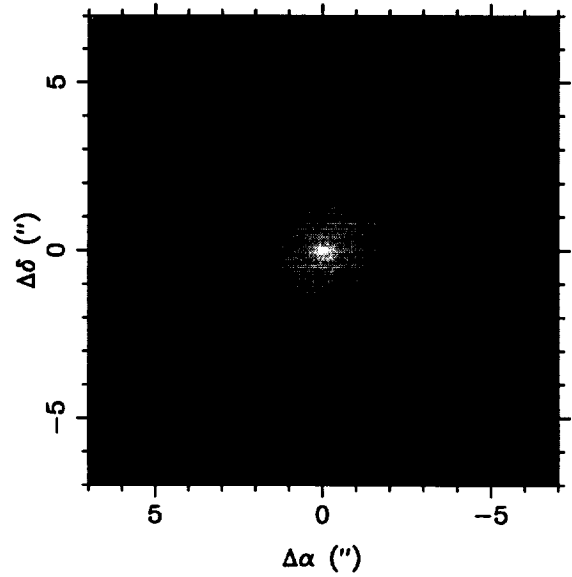
NICMOS/F110W



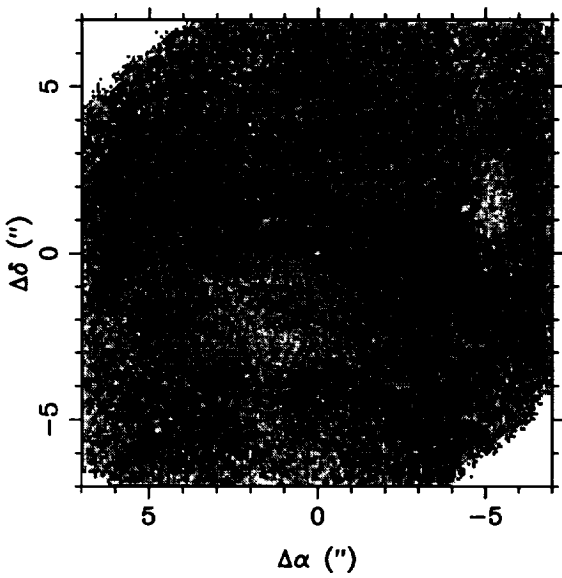
NICMOS/F160W



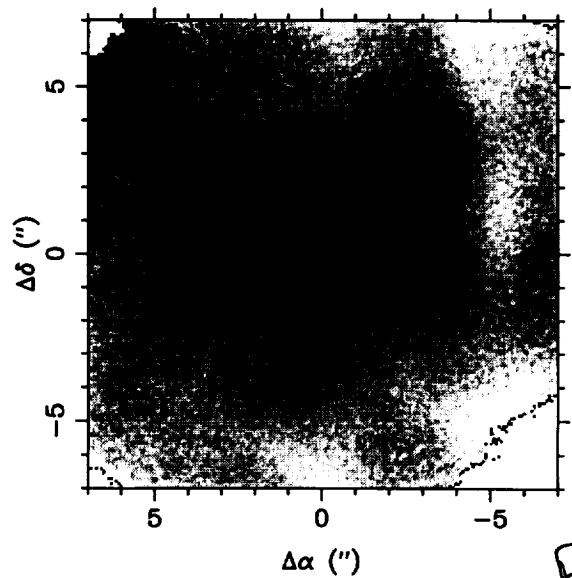
NICMOS/F205W



$(J-H)_N$



$(H-K)_N$



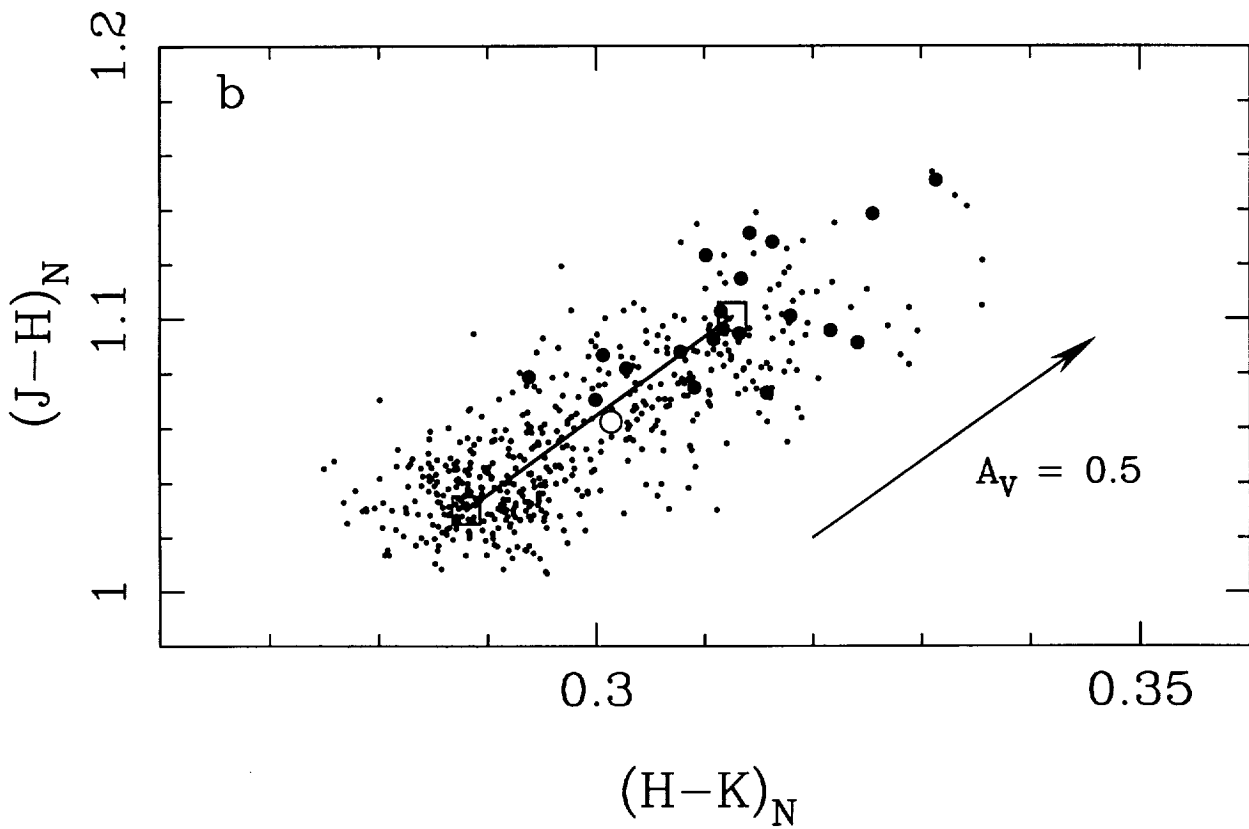
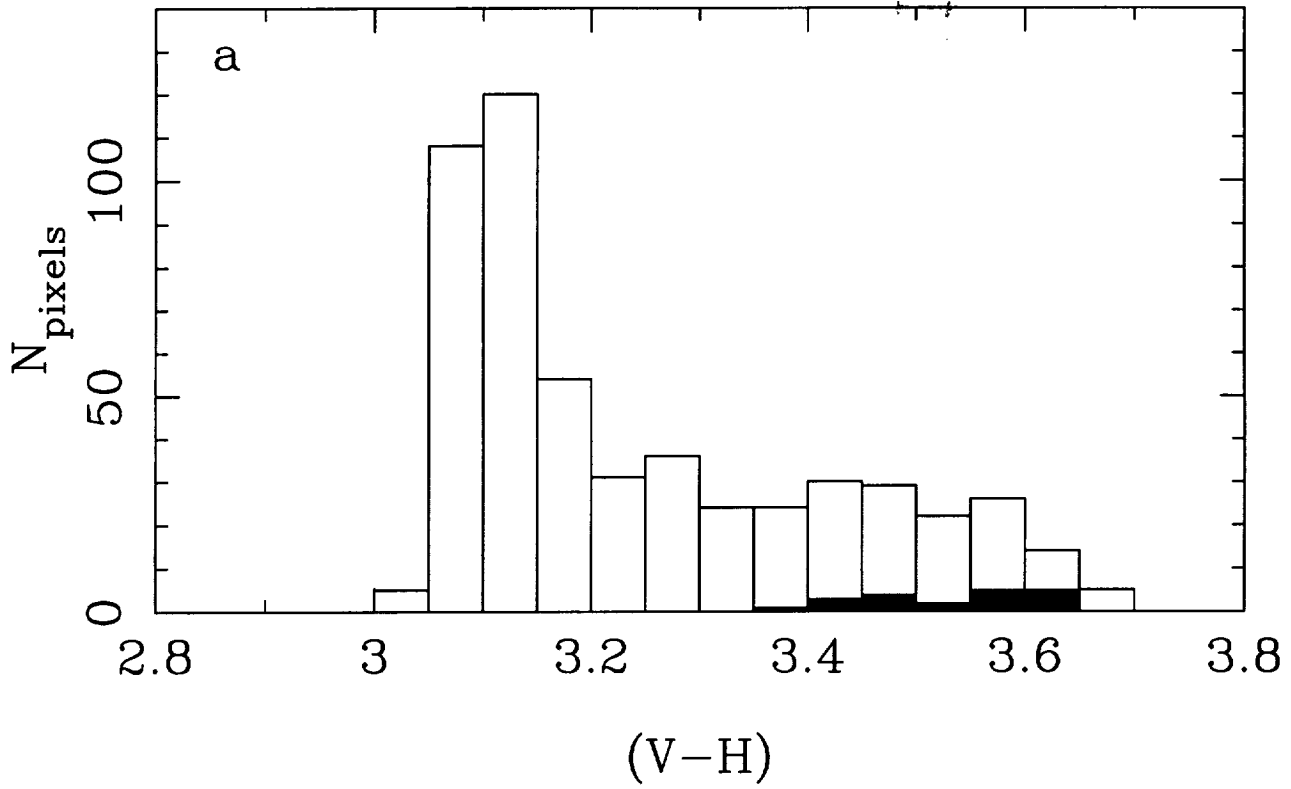


Fig. 3

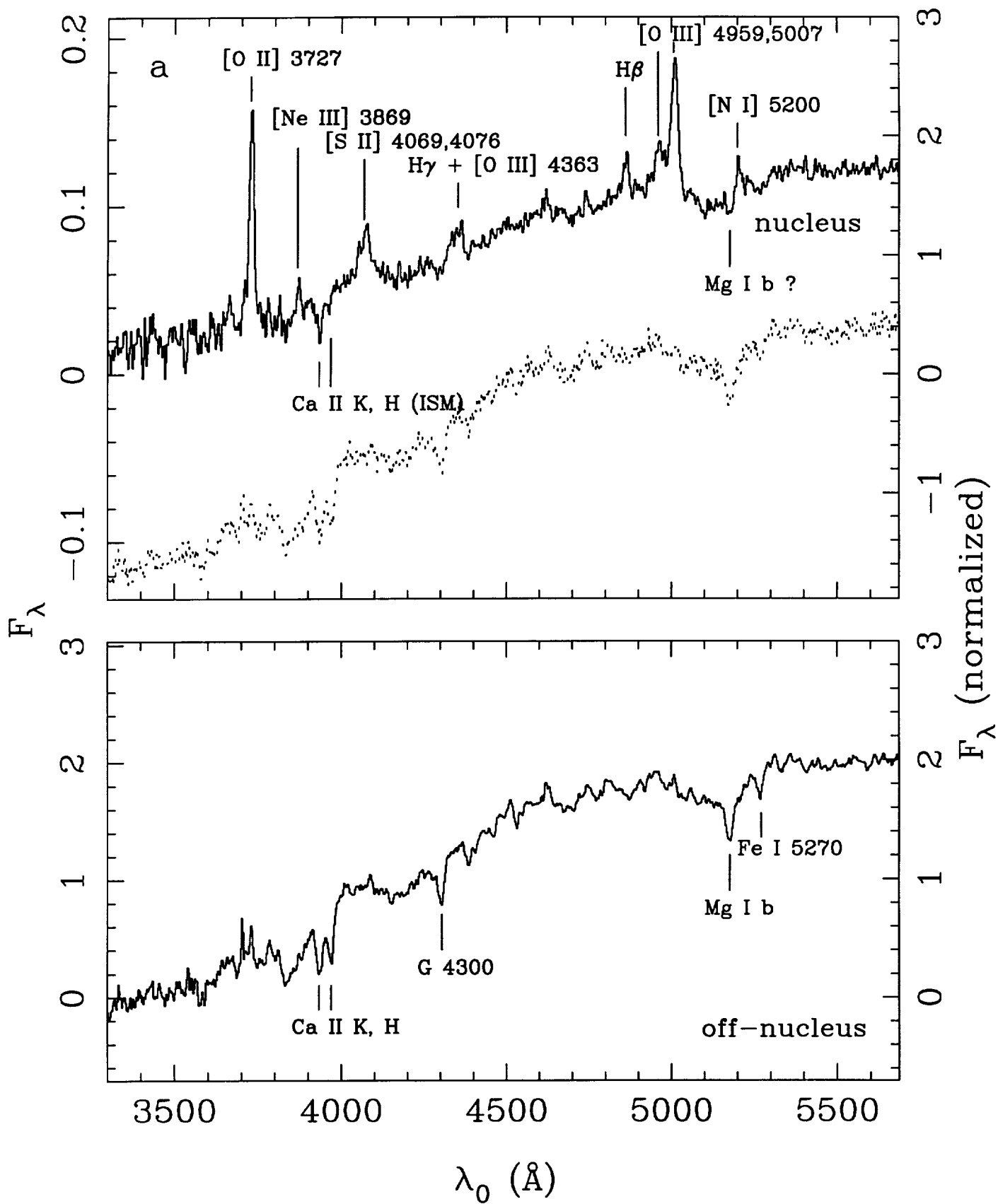


Fig. 4a

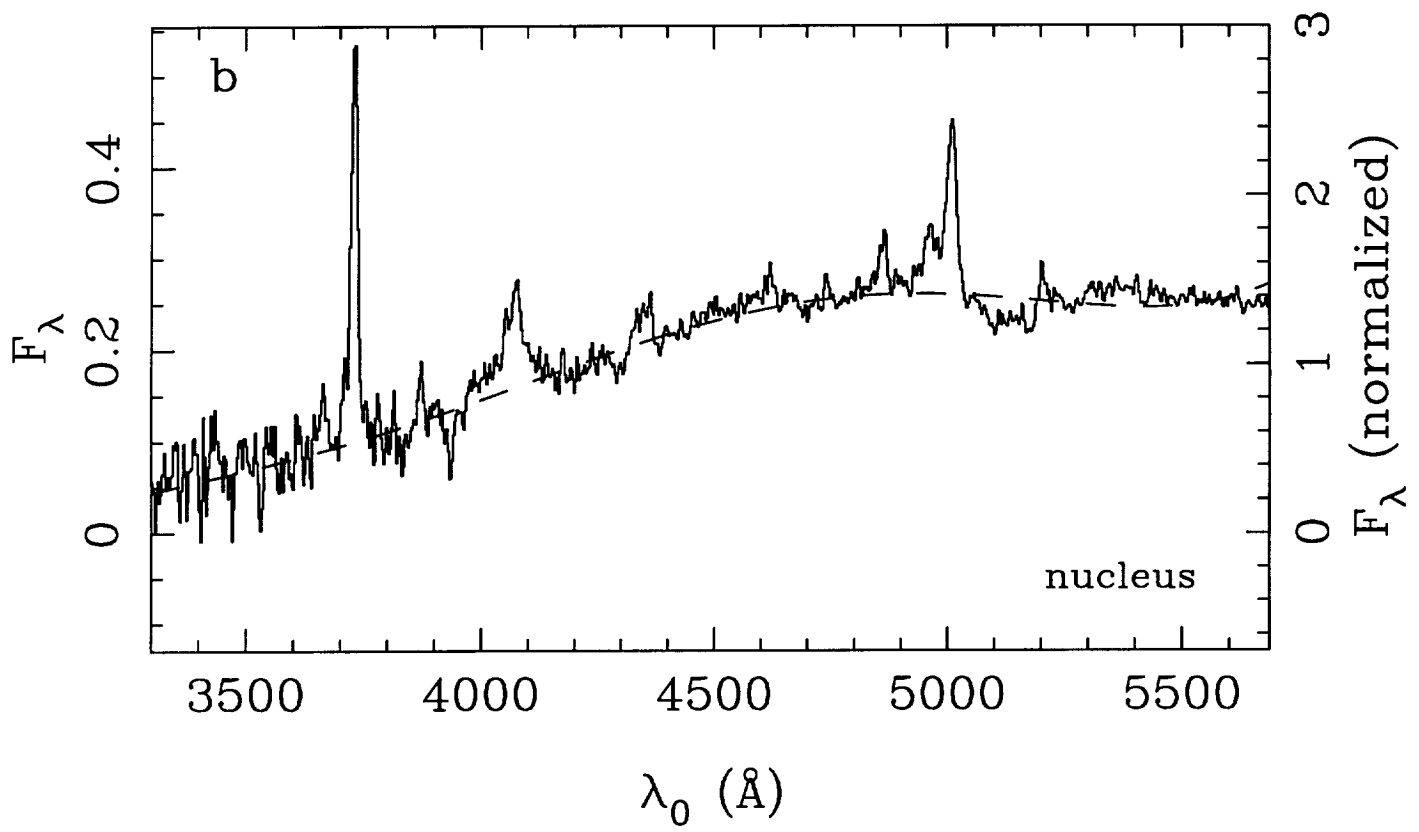


Fig. 4b

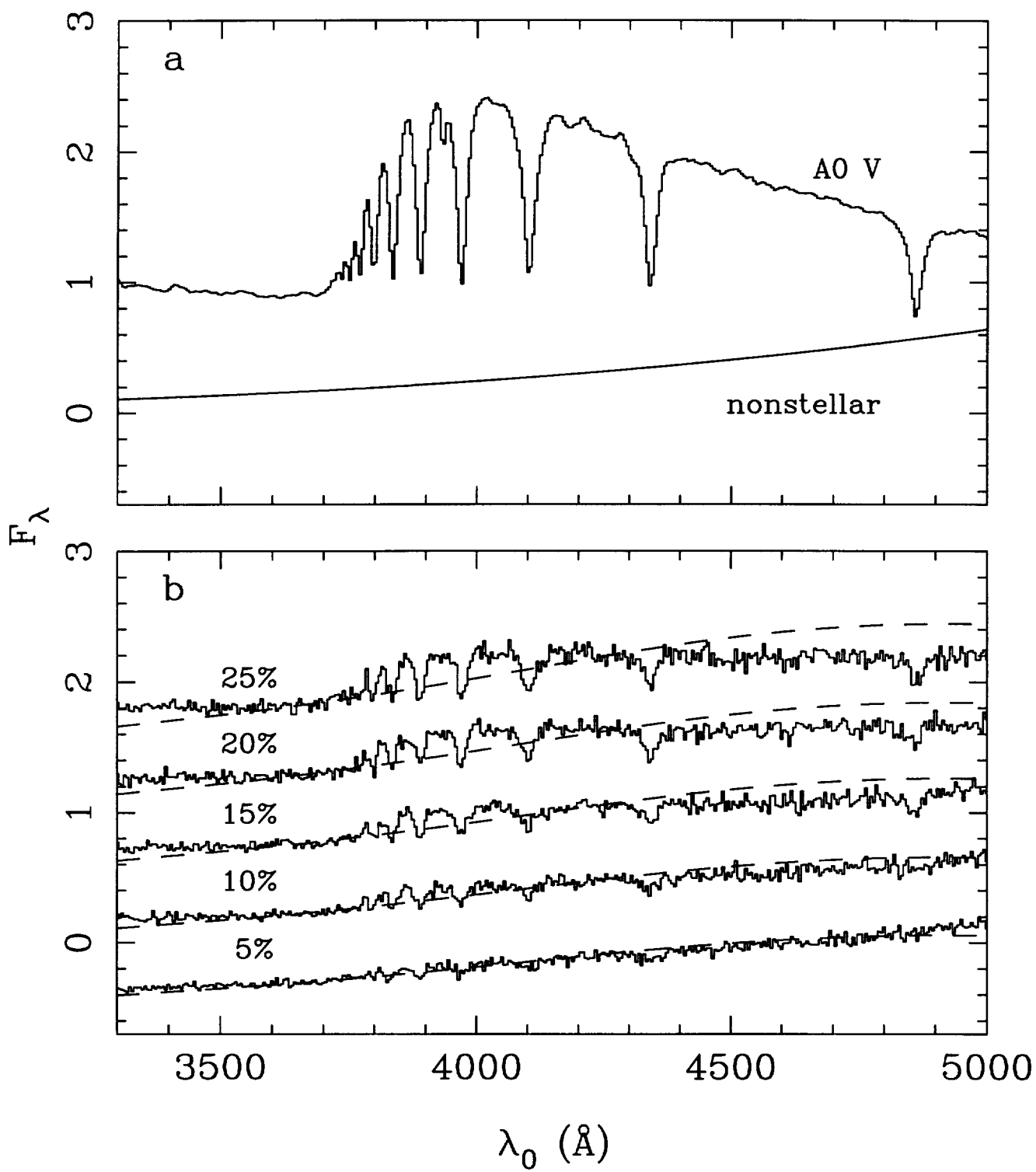


Fig. 5

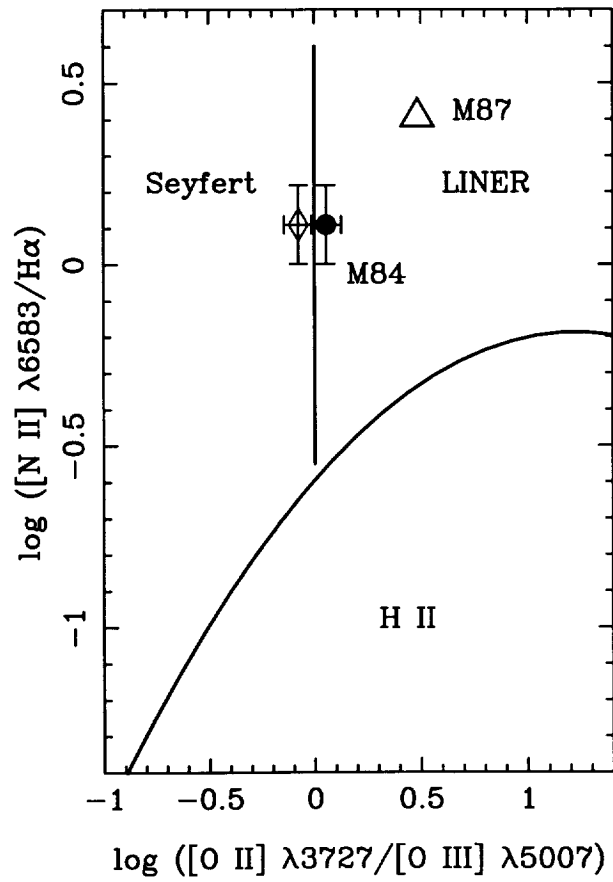
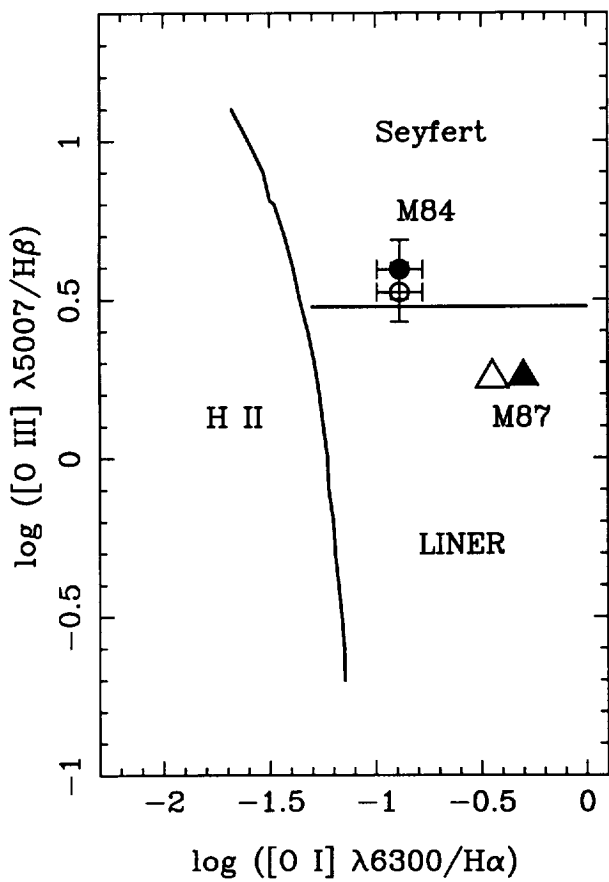
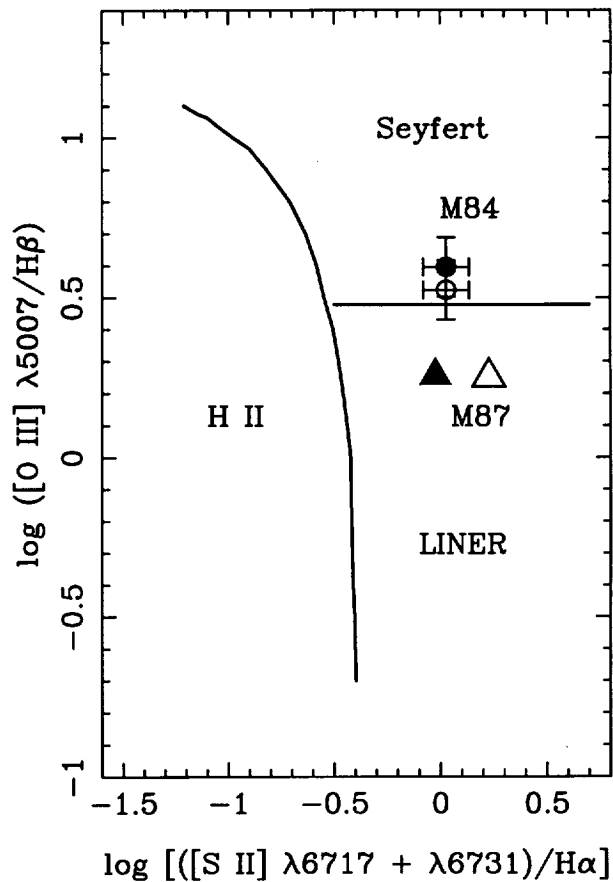
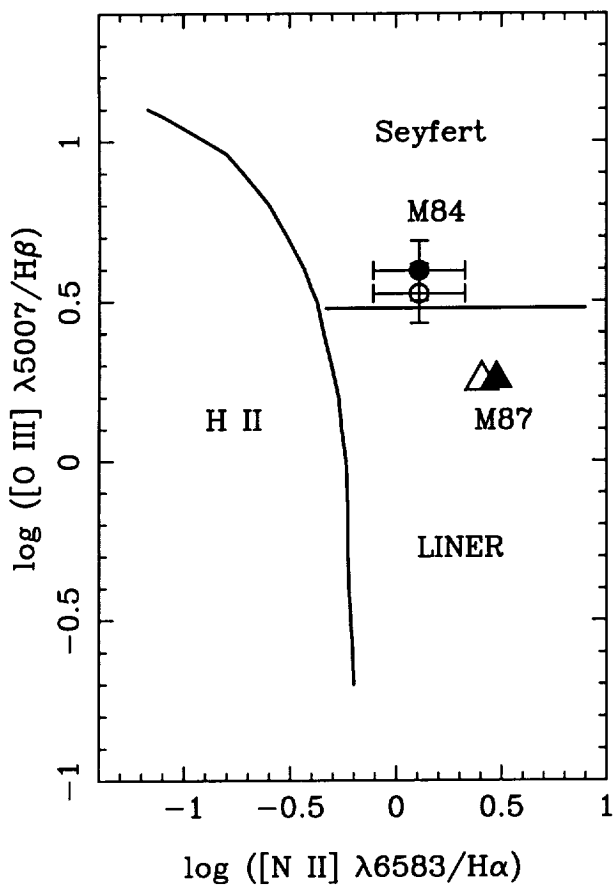


Fig. 6

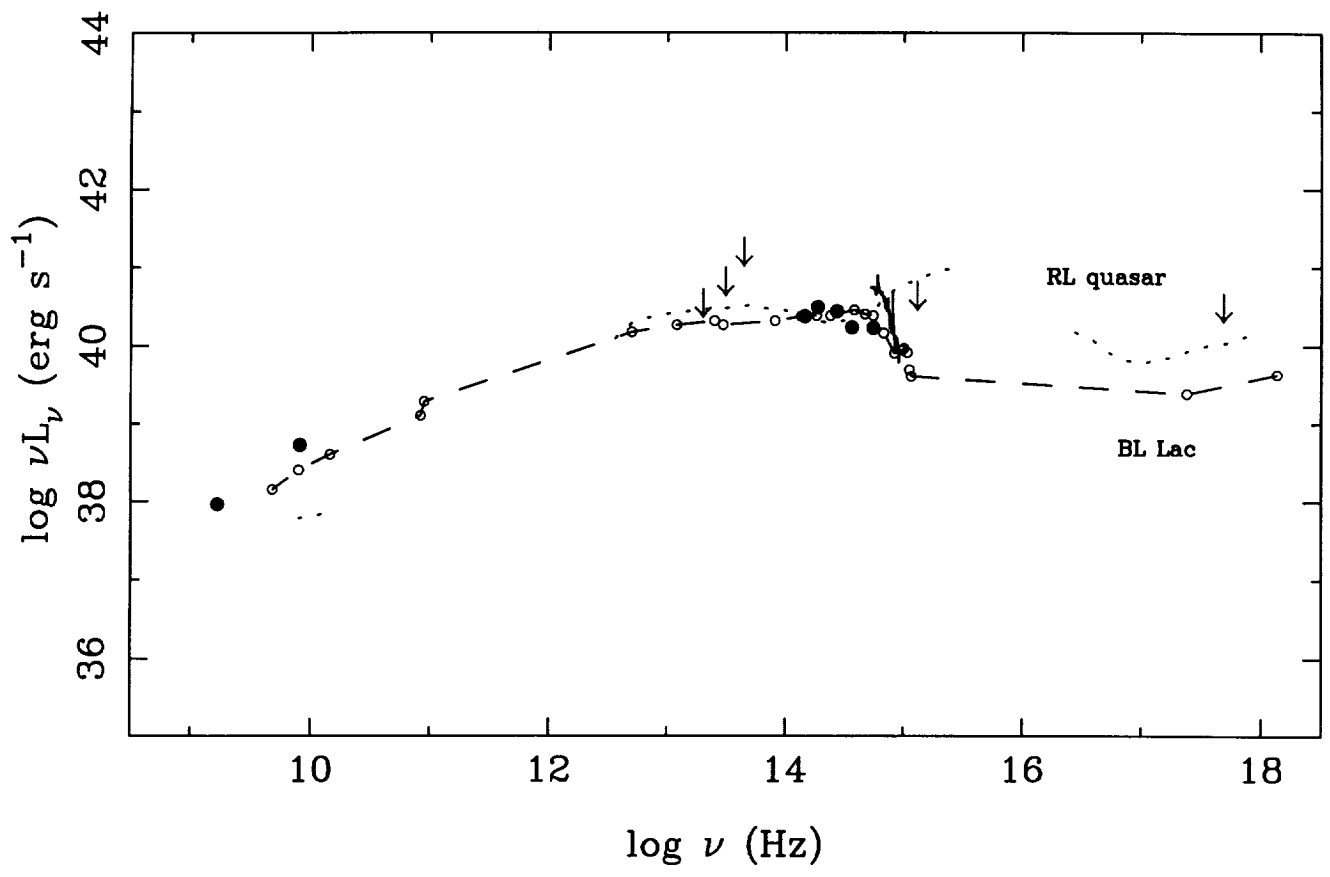


Fig. 7